Applications of metal surfaces nanostructured by ion beam sputtering

2009 J. Phys.: Condens. Matter 21 224022

(http://iopscience.iop.org/0953-8984/21/22/224022)

IOP Publishing Journal of Physics: Condensed Matter

J. Phys.: Condens. Matter **21** (2009) 224022 (17pp) doi:10.1088/0953-8984/21/22/224022

Applications of metal surfaces nanostructured by ion beam sputtering

F Buatier de Mongeot[1] **and U Valbusa**

Dipartimento di Fisica, Università di Genova, Via Dodecaneso 33, I-16136 Genova, Italy

E-mail: buatier@fisica.unige.it

Received 10 February 2009
Published 12 May 2009
Online at stacks.iop.org/JPhysCM/21/224022

Abstract

We review results relative to the formation of regular nanoscale patterns on metal substrates exposed to defocused ion beam irradiation. Particular emphasis is placed on work which demonstrates the possibility of controllably modifying chemico-physical properties of the material by tailoring the nanoscale morphology during IBS patterning. Starting from the well-established results found on single-crystal model systems, we show how the controlled modification of the atomic step termination can deeply affect chemical reactivity or magnetic anisotropy. We then look in greater detail at the more recent attempts focused on the extension of IBS patterning on supported polycrystalline metal films, a promising class of systems in view of potential applications. A modification of the functional properties of metal films can also be obtained by forcing a shape anisotropy of the nanostructures. The modification of the optical response of polycrystalline metal nanowires supported on anisotropic templates produced by IBS provides a clear example of this.

(Some figures in this article are in colour only in the electronic version)

Introduction

In this paper we review the results relative to the formation of regular nanoscale patterns on metal substrates exposed to defocused ion beam sputtering (IBS), placing particular emphasis on the work from our group which demonstrates the possibility of controllably modifying the chemico-physical properties of the pristine substrate. The functional modification proceeds either by forcing the growth of non-thermodynamic distributions of atomic steps or by inducing a shape anisotropy of the nanostructures. In section 1, after a short introduction to the basic mechanisms underlying the formation of self-organized patterns in substrates subject to defocused ion beam sputtering (IBS), we recall the peculiarities of pattern formation on crystalline metal substrates, showing the analogies and differences between IBS patterning and mounding instabilities which develop during multilayer epitaxy. On purpose this introduction is limited to the simple linear model introduced by Bradley and Harper and neglects all the sophisticated refinements of the recent theoretical models which are described in the specific contributions to this issue. In section 2 we illustrate the peculiarity of IBS for growing out-of-equilibrium and anisotropic distributions of atomic steps and we describe in which way chemico-physical properties such as chemical reactivity or magnetic anisotropy of crystalline metal substrates can be affected by modification of the local morphology. In section 3 we review results which demonstrate that it is possible to successfully extend IBS patterning from model systems (expensive single-crystal substrates) to a technologically relevant class of systems like polycrystalline metal films supported on dielectric substrates. Finally in section 4 we demonstrate that the functional properties of a (supported) metal film can be controllably modified by forcing a shape anisotropy of the nanostructures. The example provided deals with tailoring of the anisotropic optical and plasmonic response of polycrystalline metal nanowires supported on rippled glass templates via the excitation of localized plasmon resonances.

1. Basics of pattern formation during IBS processing

It is well known that, when an off-normal incidence ion beam etches an amorphous solid, a ripple or dot topography can be observed. One of the first observations was done in 1956 by Navez *et al* [1] by bombarding a glass surface with an ion

[1] Author to whom any correspondence should be addressed.

beam. They found that for incident angles close to the normal the ripple morphology is oriented in a direction perpendicular to the ion beam and that the ripple orientation is rotated by 90° when the beam is close to grazing incidence. The authors did not provide an accurate explanation at that time, but simply tried to find analogies with macroscopic phenomena like the ripple structures formed by air or water flow over a sand bed or the ripple formed after the sandblasting of solids. An explanation of the mechanism was first proposed by Bradley and Harper (BH) [2], starting from Sigmund's theory of sputtering. They proved that, since sputtering depends on the local surface curvature, under certain conditions this dependence gives rise to a surface instability where erosion is faster for the bottom of a trough than for the crest of a peak. This instability can be described by the continuum equation reported in equations (1) that describes the time evolution of the local surface height $h(x, y, t)$:

$$\frac{\partial h(x,y,t)}{\partial t} = -\nu_o + \gamma\frac{\partial h}{\partial x} + \nu_x\frac{\partial h^2}{\partial x^2} + \nu_y\frac{\partial^2 h}{\partial y^2} - D\nabla^2(\nabla^2 h) + \eta. \quad (1)$$

It is the competition between this surface instability and the smoothing effect of diffusion that forms the ripple morphology. By looking at figure 1 we can understand heuristically the mechanism of the instability proposed by BH. Ions penetrate a distance a^* inside the solid and spread their energy with a distribution which depends on the incidence angle and the crystallographic nature of the sample. The erosion velocity of a given point is proportional to the power dissipated. The energy deposited at O by ions hitting the surface at O is the same as that deposited in O′ by atoms hitting the surface in O′, but the energy deposited in O by those ions that are impinging the surface in $A(B)$ is greater than the energy deposited in O′ by ions hitting in $A'(B')$. This effect causes an increase in the velocity of erosion in O with respect to the erosion velocity in O′ and a surface instability grows. This simple picture can be described by an Edwards–Wilkinson equation in which the erosion velocity is proportional to the negative Laplacian of the local interface height $h(t)$; in a linear approximation the growth equation should be the EW equation with a negative ν, where the latter is an effective negative surface tension parameter depending on the ion beam parameters and which describes the proportionality of the erosion velocity from the local surface curvature in the direction perpendicular and parallel to the ion beam projection [3, 4].

Whenever the surface tension is negative it tends to maximize the surface in contrast to the *normal* surface tension that minimizes the surface. It is the competition between this surface instability and the smoothing effect of diffusion that forms the ripple morphology. The periodic modulation occurs along the direction for which ν is negative and, in absolute values, the largest one. The linear version of the BH model predicts that the amplitude of the preferred mode will grow exponentially with time, while the wavelength of the most unstable wave mode λ^* will remain constant at $\lambda^* = 2\pi\sqrt{2B/\nu_{\max}}$, where $\nu_{\max}$ is the maximum between ν_x, ν_y. The Bradley–Harper model, being based on a continuum approximation which neglects the atomistic details, should be considered as a simplified framework, useful for providing

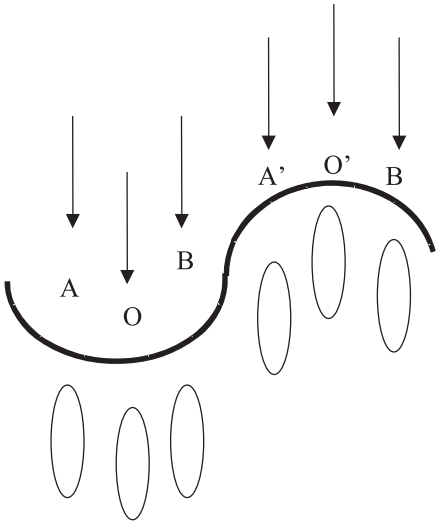

Figure 1. Schematic sketch of a modulated surface subject to ion irradiation. Energy is released in preference at the bottom of the troughs.

a coarse-grained description of the physical processes at the basis of the surface instability responsible for pattern formation during IBS. A closer agreement with the predictions of the linear version of the BH model is found for amorphous materials and for semiconductors (which get amorphized in the near-surface region) due to isotropic diffusion of the atoms displaced by the ion impact. A number of experimental observations, however, are not directly explained by the linear version of the model (e.g. non-exponential growth of the ripple amplitude, amplitude saturation, wavelength coarsening, ripple rotation as a function of ion dose) and several sophisticated refinements of the model including nonlinear terms have been developed [5, 6]. An updated reference to the more recent theoretical developments can be found in [4] and in other contributions to this issue.

1.1. IBS patterning of crystalline metals

The case of crystalline metals is more complex, since the metal surface is generally not amorphized after ion impact due to the non-directional nature of the metallic bonding. In figure 2 a scanning tunnelling microscopy topography of an Ag(001) substrate is plotted after collision of single 1 keV Ne^+ ions [7]. A characteristic pattern is formed where a vacancy cluster (central depression) is surrounded by several adatom clusters (bright islands) which are found in a radius of a few nanometres around the impact site. A similar behaviour was observed on Pt(111) by Michely *et al* [8]. A more detailed analysis of the patterns shown in figure 2 shows that the adatom and vacancy clusters are one atomic layer high/deep, indicating that the surface undergoes a recrystallization transition after the hyperthermal transient. The crystalline nature of the irradiated surface has been independently confirmed by surface diffraction experiments [9]. In the following we refer to the process of pattern formation during ion irradiation, adopting the conventional definition of ion beam sputtering (IBS) used in this issue. One should, however, keep in mind that the outcome of an ion collision process is not only the removal

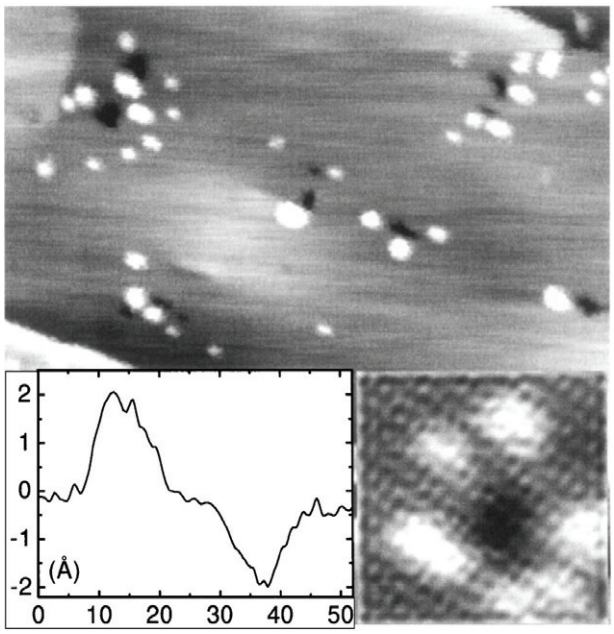

Figure 2. Top: typical surface morphology after single-ion impact experiments with 1 keV Ne^+ ions on an Ag(001) substrate held at $T = 115$ K (scan area 40×23 nm^2). Bottom right: high resolution scan of a single-ion impact pattern with software superposition of an atomic resolution image. Such images were used in order to determine the dimension of adatom and vacancy clusters. Bottom left: typical linear scan through an adatom and a vacancy cluster, demonstrating their monatomic height/depth of about 2 Å. Reproduced with permission from [7]. Copyright 2001 by the American Physical Society.

(sputtering) of a few surface atoms, but also the displacement of several adatoms and the production of vacancies.

1.1.1. The diffusive IBS regime. These results imply that, at variance with amorphous systems, on crystalline metals the diffusion of the defects (adatoms and vacancies) produced after ion collision is biased along the crystallographic directions of the substrate, independently from the geometry of the ion beam. For example, for anisotropic fcc(110) substrates like the Ag(110) case shown in figure 3, at normal ion incidence ripples can be formed with an orientation forced along the high symmetry directions [10]. For low temperature (230 K, panel (b)) the ripples are elongated along the [001] direction, at higher temperatures (320 K, panel (e)) the orientation switches by 90° to $[1\bar{1}0]$, while at intermediate temperatures (280 K, panel (c)) a chequerboard of rectangular mounds is formed. At even higher temperatures diffusion is so fast that erosion proceeds in a layer-by-layer fashion. The generality of these observations has been confirmed by experiments on other anisotropic substrates like Cu(110) [11] or Rh(110) [12].

In this context, the key role in determining the final morphology is played by temperature which governs the relative activation rate of the dominant anisotropic diffusion pathways. Additional relevant conclusions which can be derived are (i) that the pattern wavelength increases with temperature (as a result of enhanced surface diffusion) and (ii) that the pattern coarsens with sputtering time [3]. It has also been observed that the pattern wavelength in the diffusive IBS regime depends only slightly on the ion energy.

Very similar conclusions have been derived when IBS in diffusive conditions has been attempted on substrates endowed with a square symmetry like Ag(001) [10]. In figure 4 the temperature-dependent morphological evolution of the substrate is plotted for a common fixed dose of Ar^+ ions at $E = 1$ keV. The STM topographies show that for low temperatures

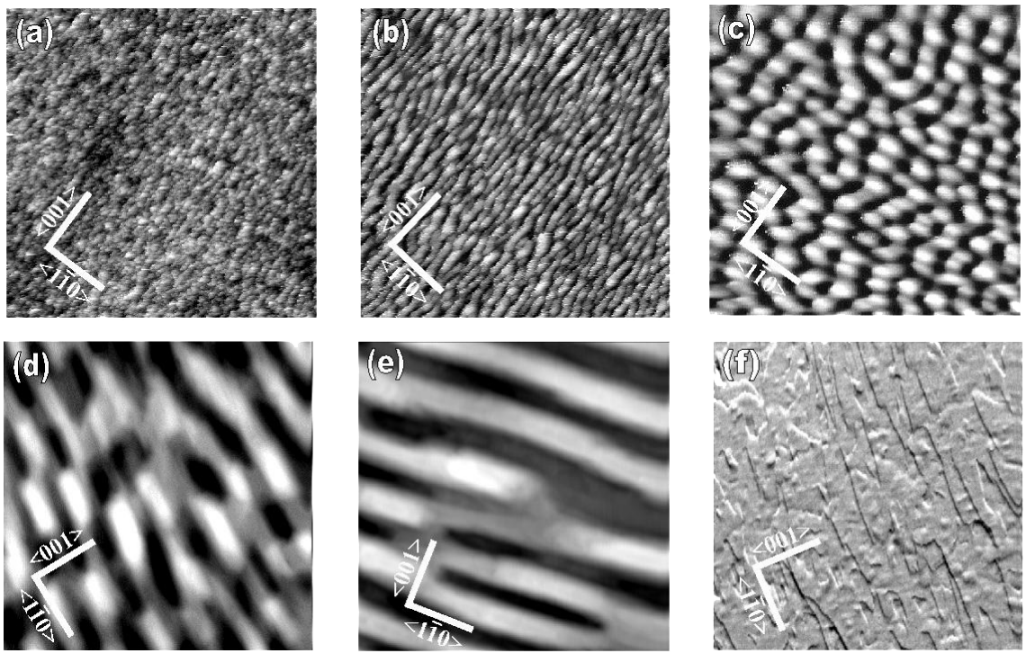

Figure 3. Six STM images (size 400×400 nm^2) of Ag(110) after Ar^+ ion sputtering (flux 4 μA cm^{-2}, $t = 15$ min) at normal incidence ($\theta = 0°$) for different temperatures. (a) 180 K; (b) 230 K; (c) 280 K; (d) 300 K; (e) 320 K; (f) 350 K. Image (f) has been acquired in derivative mode and thus appears as if illuminated from the right-hand side. Reproduced with permission from [10]. Copyright 2001 IOP Publishing Ltd.

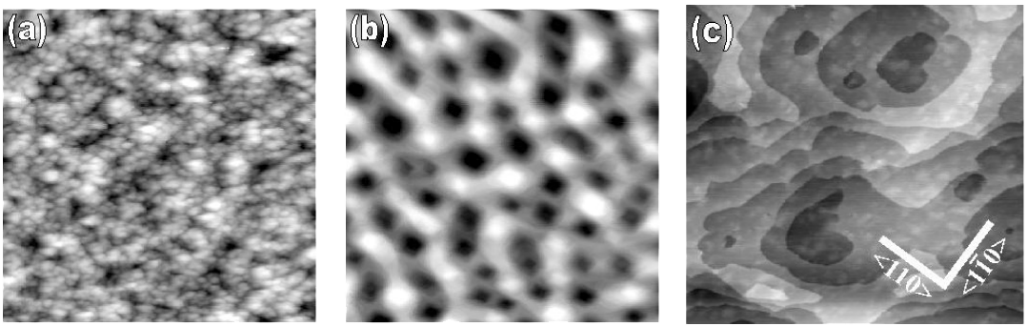

Figure 4. Temperature evolution of the Ag(001) surface morphology during diffusive IBS sputtering measured by variable temperature STM. For images (a)–(c) the experimental conditions are flux 4 μA cm^{-2}, $t = 3$ min, Ar^+ ions, $E = 1$ keV. The sputtering temperatures are: (a) 130 K; (b) 350 K; (c) 450 K. The image size is 120 × 120 nm^2 in (a), 290 × 290 nm^2 in (b) and 540 × 540 nm^2 in (c). Reproduced with permission from [10]. Copyright 2001 IOP Publishing Ltd.

(130 K, panel (a)) a randomly rough morphology is obtained due to the insufficient activation of defect diffusion, in the case of intermediate temperatures (350 K, panel (b)) square chequerboard arrays of mounds or pits with step edges aligned along the high symmetry directions are formed, and finally for even higher temperatures erosion proceeds in a layer-by-layer fashion. Finally, for fcc(111) substrates endowed with hexagonal symmetry IBS patterning under diffusive conditions results in the formation of hexagonal pits, as was demonstrated for Pt(111) [13].

1.1.2. Diffusive IBS patterning and mounding instabilities: analogies with epitaxy. The complex set of observations made for crystalline metal substrates can be reconciled if an additional destabilizing mechanism is taken into account. It originates from a constraint to surface diffusion of atoms attempting to descend step edges, the Ehrlich–Schwoebel (ES) energy barrier [14, 15]. Under diffusive IBS conditions on crystalline metals endowed with ES barriers, a preferential diffusion bias towards the uphill direction of the mounds becomes important and results in an additional destabilizing mechanism. Such ES instability (also called Villain instability [16]) was originally observed in the case of multilayer epitaxial growth, where mounded patterns resulted with characteristic periodicity and symmetry dependent on the substrate termination. With respect to the systems we have described previously, we can very briefly recall that the temperature-dependent ripple rotation during diffusive IBS patterning of Ag(110), illustrated in figure 3, has been closely replicated in a multilayer homoepitaxy experiment [17]. Analogously the mounding instability of Ag(001) leading to the formation of a chequerboard of square pyramids or pits (figure 4) could be closely replicated in temperature-dependent homoepitaxial experiments [17, 18].

The general conclusion we can draw is that IBS patterning of single-crystal metal surfaces in the *diffusive* regime is dominated by the intrinsic relaxation processes of the substrate, with preferential diffusion and incorporation of mobile species (such as atoms or vacancies) along the thermodynamically more favourable directions. The erosive action of the ion beam plays the role of a source of mobile species which reorganize themselves via thermally activated processes (similar to the role of an evaporation source in an MBE experiment, but additionally depositing vacancies) [7]. We stress that these results are specific for crystalline metals since they do not amorphize upon ion bombardment, for fluences as high as 10^{19} ions cm^{-2} and up to energies of several keV, in clear contrast to the case of amorphous or semiconductor materials (amorphized by ion irradiation) for which diffusion is isotropic and the concept of ES barrier is ill defined. For the latter systems the only source of anisotropy is thus provided by the erosive action of the ion beam impinging at non-normal incidence, as described by the Bradley–Harper model.

1.1.3. The erosive IBS regime. We now shift our attention to the erosive regime of sputtering, for which the orientation of the rippling instability is forced parallel to the ion beam projection by adopting (i) a grazing incidence sputtering geometry (incidence angles approximately above 60°) and (ii) low substrate temperatures in order to inhibit the thermally activated diffusion processes which smoothen the surface and orient the nanostructures along the preferential thermodynamic orientations [3]. The surface instability at the origin of the amplification of the parallel ripple mode is of erosive nature, analogous to the one found for amorphous materials in the BH framework; beyond a critical angle θ^* approximately above 60° the negative surface tension of the parallel mode (ν_y) becomes dominant in modulus with respect to the transverse one ν_x [2]. The evolution of the ripple amplitude and wavelength with ion dose follow a slow power law on a broad class of metallic substrates [3]. In figure 5 [3] it is shown that *erosive* IBS patterning results in the formation of an equivalent ripple pattern (wavelength in the 10 nm range) on substrates of different materials, irrespective of the orientation and crystallographic termination. Panel 5(a) refers to an Ag(001) crystal, panel 5(b) refers to Cu(110), while panel 5(c) to Ag(110). The similarity of the patterns formed in the erosive regime on substrates for which the diffusion barriers of adatoms and vacancies differ strongly is a further demonstration that the ion-beam-driven erosive instability is the predominant source of instability. Similar results have been found under extreme grazing conditions on Cu(001), with an even slower tendency to coarsening and an incipient amplitude saturation [19]; experiments performed

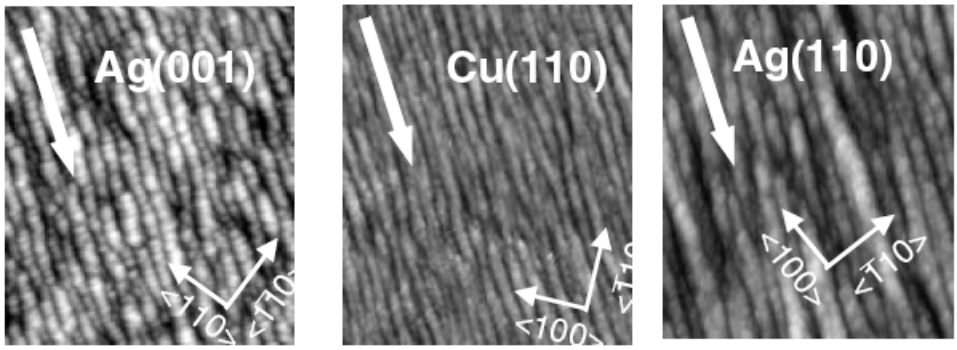

Figure 5. IBS patterning in the erosive regime ($T = 180$ K, $\theta = 70°$) of different substrates. (a) Ag(001), Ne^+ ions, $E = 1$ keV, flux 5 μA cm^{-2}, $t = 10$ min; (b) Cu(110), Ar^+ ions, $E = 1$ keV, flux 4.5 μA cm^{-2}, $t = 8$ min; (c) Ag(110), Ar^+ ions, $E = 1$ keV, flux 3 μA cm^{-2}, $t = 10$ min. Image size: 180 × 180 nm^2. Reproduced with permission from [3]. Copyright 2002 IOP Publishing Ltd.

under similar conditions on Pt(111) attribute such behaviour to an enhanced sputtering yield at the step edges illuminated by the ion beam while reflection of ions occurs on the flat terrace sites [20].

2. Functional modification of IBS nanostructured samples: the role of atomic steps

In the previous sections we have reviewed results which demonstrate that, by IBS, a flat metal surface can be destabilized, leading to the formation of regular arrays of nanostructures (ripples, mounds). Metal substrates are peculiar since they remain crystalline even after prolonged ion irradiation, thus allowing us to form regular arrangements of atomic steps, either oriented along the crystallographic orientation of the substrate (*diffusive* IBS patterning) or along the direction of the ion beam (*erosive* IBS patterning). Diffraction experiments and high resolution scanning tunnelling microscopy measurements reveal that even after prolonged ion irradiation (in the multilayer regime) the surface layers remain crystalline, indicating that the accumulation of point-like defects (adatoms and vacancies) as well as of collective aggregates (adatom and vacancy clusters) is negligible under the conditions employed in these experiments. Following the hyperthermal transient subsequent to ion impact, a high density of point defects is emitted while the surface recrystallizes. These defects can be observed in test experiments (single-ion impact) performed on flat extended terraces [7]. Under the irradiation conditions employed and due to the very high mobility of adatoms and vacancies on fcc metal substrates, for progressing ion doses the steady state density of point defects decreases due to the concurrent formation of very steep step arrays. The nanostructures formed by IBS present, in fact, a remarkable density of atomic steps, with average terraces as narrow as 3–4 atomic rows. Under these conditions, most of the surface adatoms and vacancies produced by an ion impact are efficiently annihilated at the step edges either by transient diffusion or by thermally activated diffusion. Depending on the substrate temperature, the surface morphology appears thus to be dominated either by the coalescence of the adatoms clusters to form mounded arrays (lower temperatures) or by the coalescence of vacancy clusters to form pit arrays at higher temperatures [7]. In both cases the morphology of the nanostructured profile is finally dominated by the proliferation of dense arrays of monatomic high steps.

In the following we will recall results where it is demonstrated that by IBS patterning it is possible to controllably modifying the local atomic coordination of the step edges bounding metal nanostructures, and in turn to tailor the chemico-physical properties of nanostructured substrates.

2.1. Modifying chemical reactivity by IBS nanostructuring

Growing attention has been recently devoted to the possibility of modifying the chemical reactivity of surfaces by controlling the density and nature of the defects present on them. It has been found, in fact, that surface structure strongly affects the reaction barrier for relevant chemical processes: let us mention here as examples C–H bond activation of ethane on Ir(111) [21, 22], defect-induced CO dissociation on polycrystalline Pd [23] and CO adsorption on stepped Pd surfaces [24]. More recently, point-defect-induced oxidation of graphite was reported by Lee *et al* [25] who showed that vacancies induced by ion bombardment are active for exothermal O_2 dissociation. In other works the role of surface stress and of dislocations in inducing molecular dissociation was reported [26].

The general understanding of the increased chemical reactivity of defective sites is closely related to the geometrical under-coordination of those sites and to the corresponding rearrangement of the local electronic density of states, which results in an increased charge transfer to the antibonding orbitals of the molecule [27]. In this sense atomic steps (linear 1d defects) play a similar role with respect to other kinds of defects [28].

The possibility to tune the density of atomic steps, as well as their orientation, is the key issue for tailoring, among other properties, the selective chemical reactivity of metal surfaces as well as of supported clusters. In this context, IBS nanostructuring appears as a natural choice for tuning *in situ* and in a *controlled* way the surface reactivity by producing defects (atomic steps) of a well-defined type (orientation) and density.

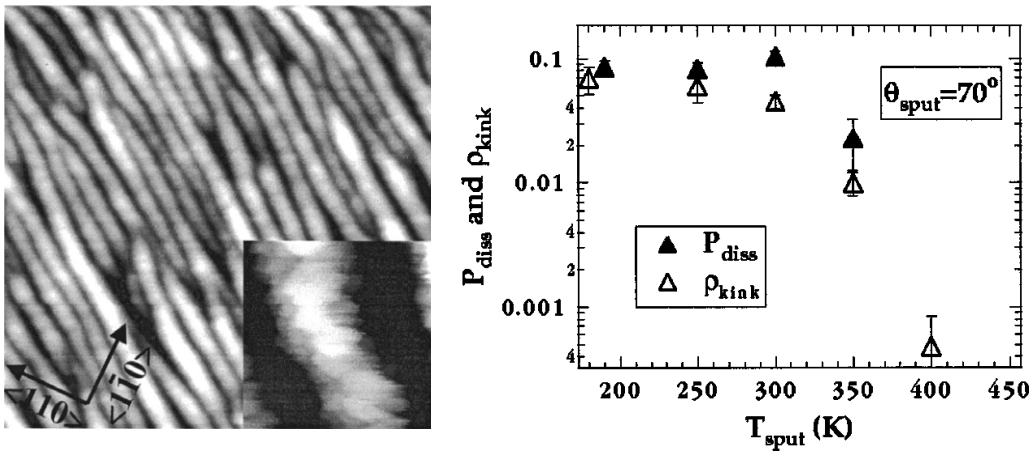

Figure 6. (Left panel) STM image (2200 × 2200 Å^2) recorded after sputtering under erosive IBS conditions at 250 K. The inset shows a high contrast magnification of the ripple edges (170 × 170 Å^2). (Right panel) dissociation probability P_{diss} (full symbols) and kink density ρ_{kink} (kink/unit cell, open symbols) as a function of the IBS irradiation temperature under erosive conditions (70° grazing incidence). Reproduced with permission from [31]. Copyright 2000, American Institute of Physics.

2.1.1. Chemical activation by erosive IBS nanostructuring: O_2 dissociation on Ag(001). In the case of O_2/Ag(001) the dissociation probability of O_2 on flat terraces is essentially negligible (below 10^{-3}) [29], but it turns out that dissociation at steps (and in particular at kinks of the [1$\bar{1}$0] steps) can be particularly efficient [30]. The possibility of tailoring *in situ* by IBS nanopatterning the density and orientation of atomic steps thus appears a natural way for increasing the reactivity of Ag(001) substrates towards O_2 dissociation [31].

In figure 6 (left panel) we show an STM topography of the Ag(001) surface subject to erosive IBS patterning, with the ion beam oriented along the [100] azimuth. The edges of the ripples in this case are forced to run along the thermodynamically unfavoured direction, which exposes the highest density of reactive kink sites. An estimate of the kink density, extracted from the local corrugation of the step edge and from the total step density on the sides of the ripples, is plotted in the left panel of figure 6 (open symbols). By increasing the substrate temperature during ion irradiation from about 200 to about 400 K, the increase of surface diffusion leads to a strong decrease in the density of thermodynamically unfavoured kinks, and the steps reorganize into a zigzag sequence of ledges oriented along the unreactive [110] termination.

The O_2 dissociation probability was derived by exposing the nanostructured substrates to a supersonic molecular beam of oxygen molecules, subsequently recording the atomic oxygen coverage by electron vibrational spectroscopy (full symbols in the right panel). It turns out that the dissociation probability scales proportionally to the density of the kink sites, and that the overall reactivity can be increased by more than three orders of magnitude. For a flat (001) terrace P_{diss} is below the experimental sensitivity (less than 10^{-3}) while it increases to more than 0.1 for the rippled morphology produced by erosive IBS patterning, when the highest density of kinks along the [001] orientation is exposed. The quantitative agreement between the dissociation probability and the density of kinks, both under grazing incidence irradiation as well as under normal incidence conditions (and for different temperatures), provides a strong direct confirmation of the dominant role of kinks (and atomic steps) for the dissociation of O_2 on Ag(001), as was independently verified in [30]. The predominant role of atomic steps in promoting chemical reactivity (and molecular dissociation) can be connected to the peculiar morphology which is induced by IBS patterning of metal substrates.

2.1.2. Chemical activation by diffusive IBS nanostructuring: CO dissociation on Rh(110) rhomboidal pyramids. While the dissociation of O_2 on the Ag(001) system can be considered as a model system, the study of transition metal (TM) substrates such as Ru or Rh appears to be far more interesting in view of applications in real-world catalysis. In this respect, CO dissociation on TM stepped surfaces and supported clusters is particularly important in heterogeneous catalysis, being one of the fundamental steps in the Fisher–Tropsch catalytic reaction, where carbon monoxide and hydrogen are converted into hydrocarbons [32, 33]. For example, it has been found that Ru atomic step sites exhibit enhanced CO dissociation activity compared to smooth (001) terrace sites [34, 35]. A strong size-dependent CO dissociation reactivity of nickel nanoclusters deposited on oxide surfaces has also been demonstrated [36]. On Rh, previous results have shown that CO dissociation is negligible on close-packed (111), (110) and (100) surfaces [37] and that it increases on stepped (211) [38] and (210) Rh substrates [39]. Experiments on Rh clusters supported on alumina surfaces have shown a strong size dependence of the reactivity towards CO dissociation [40, 41], but the nature of the active sites was not explained. It is a natural consequence of these detailed surface science studies to expect that promotion, enhancement, steering and control of CO dissociation can be reached by simply tuning surface morphology with the purpose of changing the density of reaction centres.

Rh(110) substrates exposed to IBS patterning in the diffusive regime (near normal incidence) undergo the well-established transition between a rippled state oriented along [001] at low temperatures (450 K) to a rippled state oriented

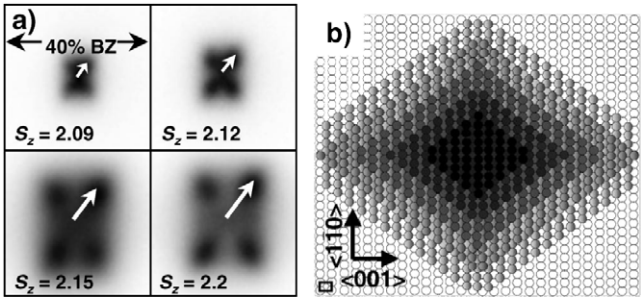

Figure 7. Structural characterization of the RP state by SPA-LEED. (a) The (00) spot is split into four satellites due to the presence of four equivalent facets. The sequence of the (00) spot profiles for increasing vertical scattering phases S_z shows that the facet spot moves away from the centre (the arrows indicate the position of one satellite) providing a measurement of the facet slope; (b) simplified cartoon of an RP island with step edges running along well-defined $[1\bar{1}2]$ directions. Darker colours correspond to topmost layers. Reproduced with permission from [12]. Copyright 2004 by the American Physical Society.

along $[1\bar{1}0]$ at higher temperatures (550 K) when noble gas ions around 1 keV energy are employed [12, 42]. These results are in close analogy to the case of other fcc(110) substrates described in section 1.1.1 (figure 3), and in the intermediate temperature range present a morphological transition state corresponding to a regular arrangement of rectangular pyramids with step edges running along the high symmetry directions. A novel kind of transition state, intermediate between the low temperature and high temperature ripples, is found when the substrate is exposed to an Xe ion beam at energies below 400 eV. As predicted in a theoretical paper [43] the rectangular mounds evolve into an array of rhomboidal pyramids (RP) bound by non-equilibrium step terminations due to the fine balance of the anisotropic diffusion currents along the two principal symmetry directions of the substrate [12, 42]. Completely analogous results have been found for Cu(110) substrates, thus confirming the generality of the finding.

In figure 7(a) the structure of the rhomboidal pyramids formed after low energy (220 eV) irradiation with Xe ions under *diffusive* conditions has been determined by high resolution electron diffraction (SPA-LEED). Under out-of-phase diffraction conditions the (00) diffraction spot appears split into four diffraction satellites, each oriented along the low symmetry direction of the respective facet. From the satellite splitting and orientation one can determine a facet slope around 11° and the step orientation corresponding to the diagonal of the unit cell. In figure 7(b) a cartoon model represents an individual rhomboidal pyramid characterized by the presence of a high density of kinked steps edges running along the $[1\bar{1}2]$ direction. Additional measurements indicate that the RPs arrange themselves into an array with lateral periodicity in the 15 nm range [42]. The rhomboidal pyramid transition state of rhodium is thus expected to exhibit the highest catalytic reactivity, since the RPs are endowed with steep facets running along non-equilibrium directions and expose a high density of under-coordinated kink atoms. In [44] the reactivity of the rhomboidal pyramid state with respect to CO dissociation

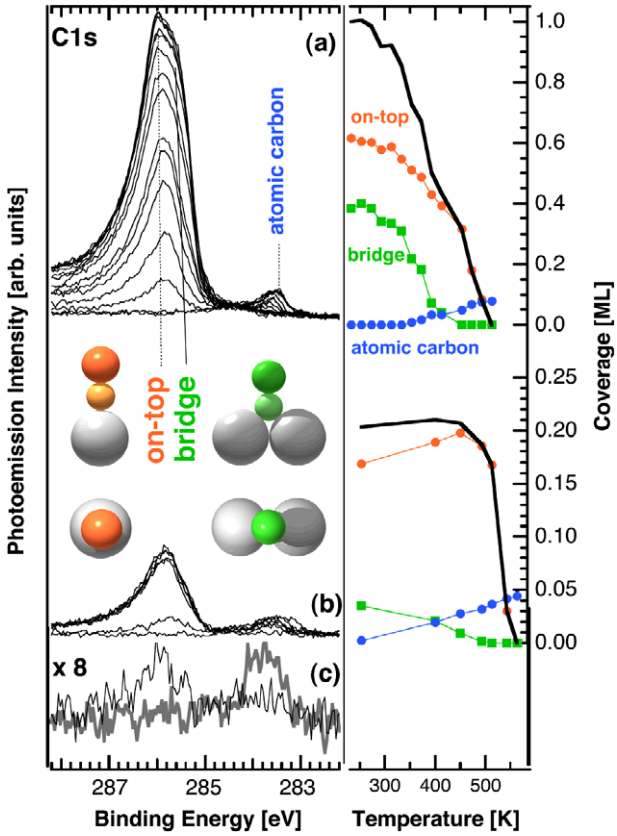

Figure 8. XPS measurement of CO dissociation on rhodium RP. (a) Left: sequence of C 1s spectra for a saturated CO layer after annealing at increasing temperature and quenching to 250 K. Right: fitted area of the C 1s peaks due to CO in on-top (light, red dots) and bridge (green squares) sites, due to total CO signal (full line) and to dissociated atomic carbon (dark, blue dots). (b) Same as above for a lower initial CO dose (0.21 ML). (c) C 1s core-level spectra for a very low CO initial dose 0.03 ML (black trace) and after annealing to 570 K (thick grey trace). Reproduced with permission from [44]. Copyright 2006 by the American Physical Society.

was studied. Figure 8 shows a sequence of XPS spectra relative to the C 1s signal of carbon measured as a function of the substrate temperature, on the rhomboidal pyramid state. Panels 8(a)–(c) refer to saturation CO coverage, intermediate coverage (0.21 ML) and very low coverage (0.03 ML). From such an analysis it is derived that the RP clusters, formed on average by about 3200 Rh atoms, have a reactivity comprised between 80% and 10% depending on the initial CO coverage. These figures compare well with the 30% reactivity of the Rh clusters of corresponding size supported on alumina [40], suggesting that the role of the alumina support is marginal and that edge effects should be dominant also for industrial catalysts.

In conclusion, these results show that Rh nanopyramids artificially prepared by IBS in the *diffusive* regime can induce the dissociation of CO, which would otherwise desorb intact on the (110) terraces. A comparison of different nanostructures prepared *in situ* by IBS [45] allows us to identify that the most probable reaction site for CO dissociation is an on-top configuration at the kinked step edges where Rh atoms have the lowest coordination.

The results shown so far have shown that by controlling the ion sputtering parameters (ion energy, incidence angle) it is possible to select the proliferation of a specific kind of atomic step oriented along a desired orientation. Another important handle for tuning the modification of chemical reactivity is given by the density of atomic steps (i.e. the slope of the facets bounding the mounds). The latter can be controlled within a limited range by simply acting on the total ion dose. A rather general trend observed in the experiments made on metal substrates show that the slope increases with a slow power law trend saturating in a range around 15°–20° which corresponds to a terrace width of 3–4 atomic rows [3, 42].

2.2. Tuning magnetic anisotropy of ultrathin films by erosive ion beam sputtering

Nanosized and nanostructured materials often exhibit electronic, magnetic and optical properties which may be very different from those of the parent bulk material. In the specific case of magnetic materials, novel properties are brought by boundary atoms which, as dimensions are reduced down to the nanoscale, give a relevant contribution to the overall magnetic properties of the system [46, 47]. Historically, ultrathin magnetic films are among the first examples of nanosized magnetic systems. Here, the altered, non-bulk-like, atomic environment affects local magnetic properties of interface atoms, such as their magnetic moment and magnetic anisotropy. By reducing the film thickness below a few tens of monolayers (ultrathin-film regime), the contribution of interface atoms to the magnetic properties of the film becomes relevant, thus leading to the appearance of extremely interesting magnetic properties [48].

For example, quasi-two-dimensional layers of Pd have been shown—contrary to the bulk paramagnetic behaviour—to be ferromagnetic [49]. Also particles of zero dimension, related to quantum well states, are reported to display ferromagnetism [50]. There are other examples in which, coming down to lengths in the nanoscale range, a substantial overturn of magnetic interactions is found; e.g. in the case of very thin Co wires, the shape anisotropy can outweigh crystalline anisotropy [51].

In view of applications, the possibility of modifying and tuning the magnetic anisotropy of ultrathin films has attracted a great deal of interest. Such interest is motivated by the fact that the magnetic behaviour of a system is greatly influenced by its magnetic anisotropy, which contributes to determining the response to external magnetic fields. In this respect, thanks to the strong sensitivity of magnetic anisotropy to interface-related symmetry breaking effects, nanostructuring gives the opportunity of tailoring the magnetic properties of ultrathin films. In ultrathin films, where the role of interface atoms is relevant or even dominant, nanostructuring therefore opens the possibility of tuning the magnetic anisotropy. In this respect, IBS has been demonstrated to be a versatile technique to induce the formation of self-organized nanosized surface structures. Particularly relevant for the tuning of magnetic anisotropy in ultrathin films is IBS in the erosive regime which induces the formation of nanoscale ripples at the surface of the film, oriented along the ion beam direction irrespective of the azimuthal orientation of the sample. The relevance of this method for magnetic applications resides in the possibility of forcing at the film surface strongly out-of-equilibrium distributions of atomic steps (which, in turn, are responsible for the rupture of the local atomic symmetry defining the magnetic anisotropy). These morphologies could not otherwise be obtained recurring to the kinetic growth instabilities which are active during MBE growth in the multilayer regime, since in the latter case the predominant step terminations are oriented along the thermodynamically preferred orientations.

Recently, we applied IBS nanostructuring to two prototypical examples of heteroepitaxial magnetic films: Co/Cu(001) [52, 53] and Fe/Ag(001) [54, 55]. For both these systems, erosive IBS was found to induce the formation of nanosized surface ripples parallel to the ion beam projection, analogously to the case of single-crystal metal surfaces. The rippled surface morphology has a strong impact on the magnetic anisotropy of the films and, in particular, it induces a uniaxial contribution to the in-plane magnetic anisotropy. The evolution of the anisotropy strength and of the nanoscale morphology as a function of the ion fluence has been exploited to identify the different contributions (magnetocrystalline and magnetostatic) to the induced magnetic anisotropy.

In the above-mentioned experiments, sputtering was performed along the azimuthal direction of the thermodynamically preferred steps (namely along the [110] directions of fcc Co and the [100] directions of bcc Fe). In this configuration, the development of the ripple structure induces the imbalance of the densities of steps parallel and perpendicular to the ripples' ridges. In fact, since the sidewalls of well-developed ripples consist in a staircase of terraces separated by monatomic steps, the steps oriented parallel to the ripples' ridges become more abundant than the ones oriented perpendicular to them. At variance with atoms at terrace sites, which are affected by a biaxial magnetic anisotropy in the plane of the film, atoms located at step sites are endowed with a uniaxial anisotropy with easy axis parallel or perpendicular to the step edge, as pointed out by experiments performed on magnetic films deposited onto vicinal substrates [56, 57]. Therefore, at low ion fluences, the step imbalance generated by the ripple structure can be identified as the origin of the uniaxial magnetic anisotropy in ion-sputtered Co/Cu(001) and Fe/Ag(0 01) ultrathin films.

With regard to the first system, due to the quasi-ideal layer-by-layer growth of Co films deposited at room temperature on Cu(001) substrates, Co/Cu(001) was frequently chosen as a prototype to study the magnetic properties of ultrathin films. As shown in figure 9(a), at room temperature, the growth of 12 ML of Co on Cu(001) proceed in a quasi-layer-by-layer mode, exposing in the topmost layer square islands with steps oriented along the high symmetry [110] directions. In figure 9(b), the hysteresis loops obtained by means of longitudinal MOKE measurements for the 12 ML thick Co/Cu(001) film are plotted for H oriented along the two equivalent easy axis directions (parallel to the step edges): the hysteresis loops present an identical sharp square shape revealing that the film presents equivalent

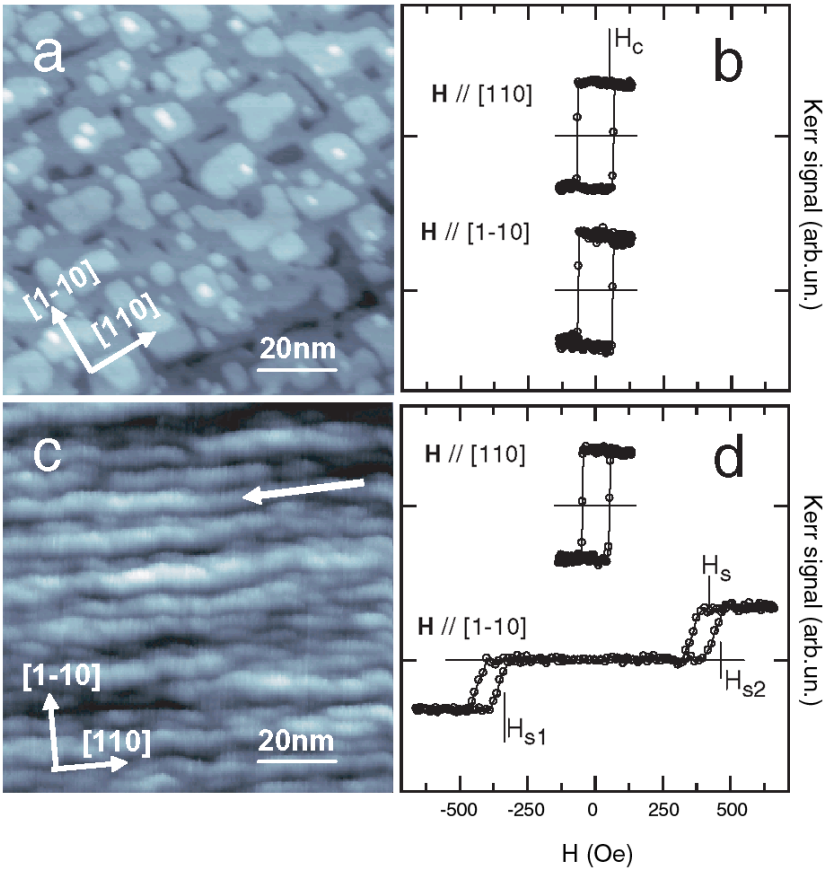

Figure 9. (a) STM image and (b) hysteresis curves of the flat 12 MLE thick Co/Cu(001) film. (c) STM image and (d) hysteresis curves of the Co film after erosive IBS nanostructuring with an ion dose of about 12 MLE. The arrow indicates the projection on the surface plane of the ion beam direction. Reproduced with permission from [52]. Copyright 2003 by the American Physical Society.

distributions of atomic steps bounding square islands. Grazing incidence (erosive) ion sputtering was then performed along the azimuthal [110] directions which correspond to the orientation of the thermodynamically preferred steps at the (001) surface of fcc Co (figure 9(c)), leading to the formation of well-defined ripples (wavelengths in the range of the order of 10 nm) in analogy to the case of the single-crystal substrates (similar power law trends for wavelength and for roughness). Following IBS patterning, the magnetic properties of the film and, in particular, its magnetic anisotropy resulted in being profoundly modified. In figure 9(d) the hysteresis loops parallel and perpendicular to the nanowire axis are shown after a sputtering fluence equivalent to 12 ML.

A uniaxial contribution to the pristine biaxial magnetic anisotropy of the Co/Cu(001) film develops in the plane of the film. The resulting magnetic anisotropy of the nanostructured film therefore exhibits an easy and an intermediate axis, respectively parallel and perpendicular to the ripple ridges, and a hard axis in between the two. The hysteresis loops measured with the external magnetic field along [110], that is parallel to the ripple ridges (easy axis), remain square in all the investigated fluence range, indicating that the IBS process did not modify significantly the crystalline environment of the Co atoms forming the ripples.

The modifications of the magnetic anisotropy strongly affect the shape of the hysteresis loops measured with the external magnetic field parallel to the intermediate axis: the shape moves from the square one of the as-grown film to a double split-semiloop shape. The semiloops are characterized by well-defined and sharp irreversible transitions and the strength of the uniaxial contribution to the in-plane magnetic anisotropy can be simply related to separation in the magnetic field of the two semiloops (shift field) [58].

A key feature of the IBS nanopatterning is represented by the possibility of continuously varying *in situ* the magnetic anisotropy of the nanostructured film by simply acting on the ion dose. This is clearly shown in figure 10 where the hysteresis loops recorded for H oriented along the $[1\bar{1}0]$ direction are plotted as a function of the ion dose with the ion beam along [110]. The shift field of the semiloops, which is directly related to the magnetic anisotropy, increases monotonically with ion dose. The change in the magnetic behaviour is directly related to the modification of the distribution of atomic steps, with a proliferation of steps running along the [110] direction as shown in the corresponding STM images [53]. Further increasing the ion dose, the amplitude of the Co ripples progressively grows, while the average thickness of the residual film decreases due to ion etching, until the rippled cobalt film decomposes into an array of disconnected nanowires supported on the Cu(001) substrate. In correspondence to the disconnection of the nanowires the magnetostatic (shape) contribution to the

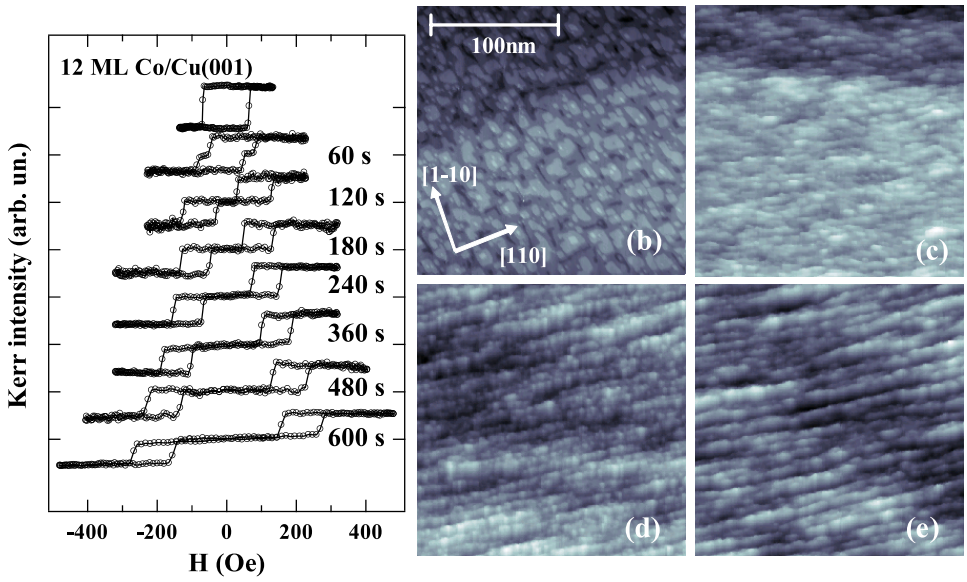

Figure 10. (a) Longitudinal MOKE hysteresis loops for a 12 ML thick Co/Co(001) film patterned by erosive IBS along the [110] direction. The external magnetic field is parallel to the $[1\bar{1}0]$ direction. The loops have been normalized at saturation. Ion fluences are reported on the graph. (b) STM images (200×200 nm^2) of the flat Co film and after ion irradiation for (c) 60 s, (d) 660 s and (e) 960 s. Reproduced with permission from [53]. Copyright 2003, American Institute of Physics.

overall magnetic anisotropy becomes dominant with respect to the magnetocrystalline one [52, 53].

The general applicability of erosive IBS for tuning magnetic anisotropy was verified on a second prototypical example of an ultrathin magnetic system, Fe/Ag(001). This choice was motivated by the good epitaxial growth resulting in the small lattice mismatch (about 0.8%) in the plane of the film, despite the large mismatch in the lattice constants, through the 45° rotation of the Fe(001) plane with respect to the Ag(001) plane. It was thus possible to use erosive IBS for investigating the magnetic anisotropy of monatomic steps at the surface of Fe/Ag(001) films [54, 55]. The possibility of isolating and determining the magnetic anisotropy of steps is particularly relevant since other approaches conventionally used to address this goal, as the growth on vicinal surfaces, proved unsuccessful for Fe/Ag(0 01) films. The reason of this failure resides in the peculiar epitaxy of Fe films grown on Ag(001) which, despite the small in-plane lattice mismatch, produces a large vertical mismatch. Such vertical mismatch, of nominally 30%, generates a significant strain in the Fe film in the neighbourhood of monatomic Ag steps which, in the case of films grown on vicinal Ag(001) surfaces, gives rise to a uniaxial anisotropy of magnetoelastic origin. Such bulk-like magnetoelastic contributions previously prevented the assessment of the role of surface steps to magnetic anisotropy [59]. Following IBS patterning in the erosive regime along the azimuthal [100] direction of Fe films on Ag(001), a strong uniaxial anisotropy was found to develop. In the low-fluence regime, the origin of the uniaxial anisotropy was identified, analogously to the case of Co/Cu(001), with the imbalance in the number of thermodynamically preferred steps oriented along and perpendicular to the sputtering direction produced by the IBS process.

A natural extension of the above reported results has been to apply ion beam sputtering for the modification of the magnetic anisotropy of supported polycrystalline films of ferromagnetic materials [60, 61]. The experiments demonstrate that also in this case the isotropic magnetization of the flat film can be transformed to uniaxial in correspondence to the formation of the anisotropic ripples induced by erosive IBS patterning at grazing incidence. For polycrystalline films the origin of the magnetic anisotropy has, however, more to do with the magnetostatic terms (shape anisotropy) rather than with the magnetocrystalline terms since in polycrystalline films the orientation of individual grains is random and no preferred step termination can be selected, as was the case for epitaxial films.

Recently, a major company involved in magnetic data storage has issued a patent in which the ideas outlined above have been implemented to develop a high performance magnetoresistive sensor head optimized to perform high density data storage [62]. The magnetoresistive sensor has a hard magnetic pinning layer with an engineered magnetic anisotropy in a direction substantially perpendicular to the medium-facing surface. The hard magnetic pinning layer may be constructed of CoPt, CoPtCr or some other magnetic material and is deposited over an underlayer that has been produced by IBS. The ion beam etch has been performed at grazing angles with respect to normal in order to induce the formation of anisotropic roughness, for example in the form of oriented ripples or facets oriented along a direction parallel to the medium-facing surface. The anisotropic roughness induces a strong uniaxial magnetic anisotropy substantially perpendicular to the medium-facing surface in the hard magnetic pinning layer deposited there.

3. IBS Patterning of polycrystalline metal substrates: role of topographic roughness and of grain boundaries

The results reported so far are mainly focused on the application of IBS nanostructuring to model systems,

i.e. single-crystal metal substrates, or flat epitaxial metal films which grow in a quasi-layer-by-layer mode. Due to the cost of the substrates and to the time-consuming UHV cleaning cycles required to prepare atomically flat extended terraces, these results cannot be considered of immediate interest in view of the implementation into functional devices.

In most applications dealing with functional metal coatings, e.g. magnetic storage devices, IC interconnects and advanced optical coatings, the metal overlayer is deposited in polycrystalline form. Since a polycrystalline metal film is composed by individual grains which present a random distribution of orientations, the coherent development of a pattern with long range recurring to *diffusive* IBS patterning appears unlikely. The development of the surface instability involves thermally activated diffusion of mobile adatoms and vacancies, thus giving rise to a *local* preferential orientation of the pattern according to the texture of the individual grains. This fundamental difficulty, intrinsic to polycrystalline metal systems, can be overcome recurring to IBS patterning in the erosive regime: the symmetry of the ripple, forced by the projection of the ion beam at glancing incidence, turns out to be independent of the local orientation of the individual grains, provided the temperature of the substrate is kept sufficiently low to hinder thermally activated diffusive relaxation.

Some preliminary reports have shown the possibility of patterning polycrystalline thin metal films by means of defocused ion beams [60, 63, 64]: however, the crucial role of initial surface morphology has been so far overlooked. These issues have been addressed in a recent paper [65] in which the formation of ripples by erosive IBS sputtering has been studied as a function of the polycrystalline morphology (grain size and roughness) of Au films deposited on glass slides.

In order to extend the results found on single-crystal model systems to polycrystalline films, the influence of the vertical and lateral corrugation of the pristine film morphology (*topographic roughness*) on the dynamics of the self-organization process was studied. In the case of near-grazing ion irradiation conditions (*erosive* IBS patterning), the spatial distribution of ion impact sites can be biased by the vertical and lateral distribution of the initial surface morphology (via shadowing effects). This can be seen with the aid of figure 11 where an AFM line scan across a 150 nm thick polycrystalline Au film deposited on a glass slide is shown. The vertical scale of the graph has been expanded, so that the ion beam impinging at an 82° grazing angle (arrows) appears more to the normal. In the initial stages of ion irradiation, the taller grains prevent the ion beam from reaching the shallower ones behind them, thus providing a self-levelling mechanism which propagates the dominant topographic features in the direction of the ion beam. Such a spatial modulation of the ion impact sites (not present in the case of *erosive* IBS on flat films) triggers a shadowing instability in the early stages of ion irradiation. In addition to the topographic roughness, the presence of grain boundaries (GBs) can also affect the evolution of the self-organized patterns. Diffusion of adatoms and vacancies could, in fact, be hindered in the presence of GBs, since they impose a characteristic length scale for lateral mass transport which depends on the grain size.

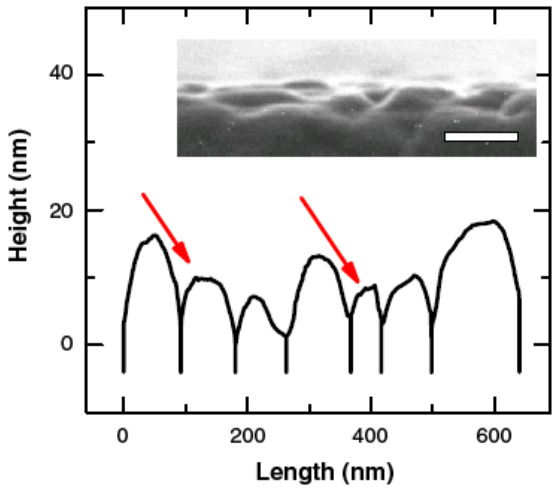

Figure 11. AFM line profile of a 150 nm thick polycrystalline Au film grown by thermal evaporation (vertical scale amplified). The arrows represent the ion beam impinging at 82° with respect to the surface normal. A representative cross-sectional SEM micrograph is shown in the inset, scale bar 100 nm. Reproduced with permission from [65]. Copyright 2008 by the American Physical Society.

In figure 12 a sequence of SEM images demonstrates that the distribution of grain sizes of polycrystalline Au films can be varied in a broad range by adopting different growth procedures. In all cases, as is typical for fcc metals, a predominant (111) in-plane texture is observed. For sputter-deposited films (panel (a)) the grain distribution is peaked around 70–80 nm, for thermally evaporated films (panel (b)) the peak of the grain size distribution shifts to slightly higher values, around 90–100 nm, and at the same time a non-negligible population of anomalous grains with sizes around 130 nm is found, finally for the flame annealed films (panel (c)) the grain extension increases significantly to the micrometre range, i.e. well above the typical lateral wavelength of the nanostructures produced by IBS on metals (in the 100 nm range).

The polycrystalline Au samples have been exposed to defocused IBS irradiation under erosive conditions (grazing sputtering angle $\theta = 82°$) from a gridded multiaperture Ar^+ source with the substrate held near room temperature. Figures 12(d)–(f) show representative AFM images of the different Au surfaces irradiated with the same intermediate ion dose of 7×10^{17} ions cm^{-2}. Ripples grow parallel to the ion beam projection with an elongation inversely proportional to the roughness of the pristine film. Measurements of the average ripple wavelength show that after ion irradiation a well-defined elongation in the beam direction is visible and the estimated value of the ripple periodicity can vary from $\Lambda \sim 70$ nm (sputter deposition) to $\Lambda \sim 120$ nm (thermal deposition). These periodicities are in quantitative agreement with the lateral size distribution of the dominant grains in the pristine samples described in figures 12(a) and (b).

The situation is completely different when patterning the film of figure 12(c) (flame annealed Au) which has grain sizes in the micrometre range, well exceeding the typical ripple wavelengths. In this case each of the grains locally behaves as a flat monocrystalline Au(111) surface and the dynamics

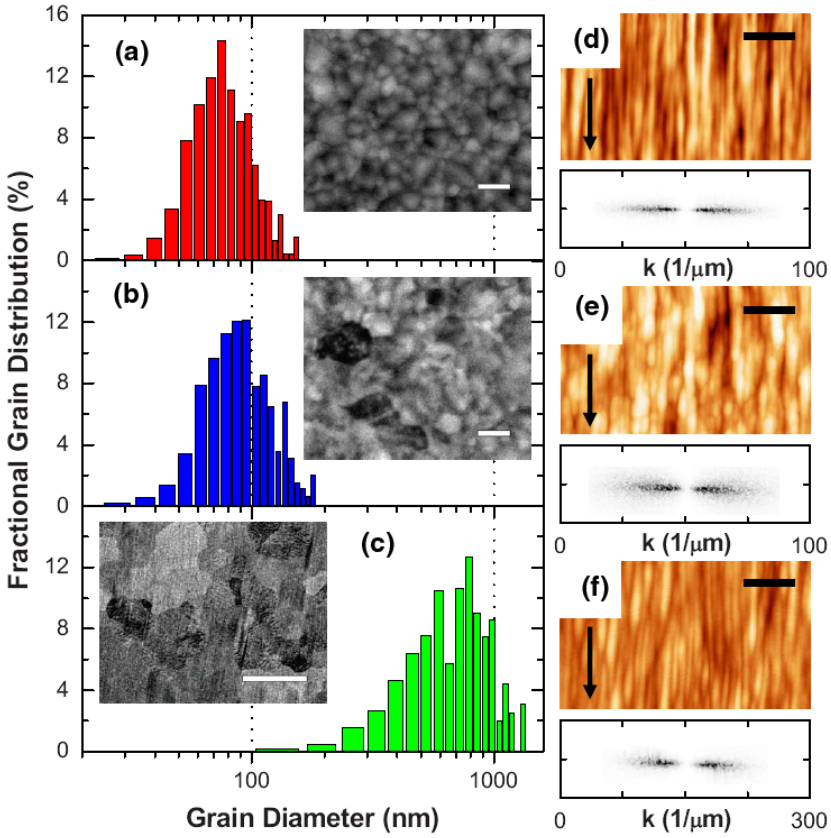

Figure 12. Grain size distribution (fractional surface coverage) of the Au films obtained from SEM imaging. The 150 nm thick films were grown by different procedures: (a) sputter deposition, (b) thermal evaporation, (c) flame annealing. The SEM scale bars are, respectively, 100 nm, 100 nm and 1 μm. (d)–(f) AFM images of the Au films in ((a)–(c)) after erosive IBS irradiation at the same dose 7×10^{17} ions cm^{-2}. Insets: 2D FFT of the AFM images. The AFM scale bars are 600 nm for ((d) and (e)) and 200 nm for (f). Reproduced with permission from [65]. Copyright 2008 by the American Physical Society.

of the rippling instability follows a slow monotonic increase of wavelength and ripple amplitude as is typical for IBS patterning of single crystals in the erosive regime (grazing incidence conditions). For the AFM image in figure 12(f) the wavelength amounts to $\Lambda \sim 30$ nm, a value compatible with the results found on single crystals [3].

The nonequivalence of the ripple pattern (wavelength and elongation) on films with non-flat initial morphology, after irradiation with the same ion dose, provides a clear indication that, under glancing angle irradiation conditions, the non-stochastic spatial modulation of ion impact sites imposed by the vertical grain distribution is playing a key role (shadowing mechanism). In this way, the size of the dominant topographic features of the pristine film imposes the wavelength of the incipient ripple pattern.

Further nontrivial conclusions can be derived if one compares the evolution of the ripple pattern on the different substrates at higher ion doses (figure 13). (i) There is an initial decreasing trend of Λ for the rough films (full and open squares) in correspondence to the elongation of the ripple ridges. This decreasing trend has been qualitatively interpreted with the aid of the BH linear model which predicts the existence of an *intrinsic* wave mode growing faster than all the other ones. As shown in figure 13(b), the intrinsic BH wavelength found for flat single-crystal-like films (filled triangles) is well below the initial wavelength imposed by the shadowing instability on the rough films. Thus for increasing ion doses the BH instability amplifies more the wavemodes at smaller wavelength, shifting downwards the overall distribution [66]. (ii) At longer sputtering times a crossover to the conventional IBS erosive regime observed for single crystals (power law increasing trend of Λ) is observed in figure 13(b). The twofold reduction in the ion dose required for the formation of equivalent ripples for the rough films (full and open squares) in comparison to the case of a flat surface (filled triangles) is significant. This can be easily recognized in the insets of figures 13(a) and (b) which show that a horizontal rigid shift of the data relative to the non-flat films (open and filled squares) by $\Delta\Theta = +1.2 \times 10^{18}$ ions cm^{-2} leads to a collapse of the data points (both of Λ and of h) over the single-crystal erosive curve (filled triangles). These observations imply that, for an initial topography possessing wavemodes that are amplified within the BH linear model, the subsequent evolution is receiving a head start with respect to the flat initial case [66]. The primitive roughness of the polycrystalline film thus efficiently reduces the ion dose required for the formation of equivalent ripple modulations on a flat film.

(iii) Grain boundaries represent a barrier which hinders inter-grain mass transport, a limiting factor for the coherent elongation of ripples. Additionally, the different crystallographic orientations of adjacent grains impose a local anisotropic diffusion bias to the mobile species, a further

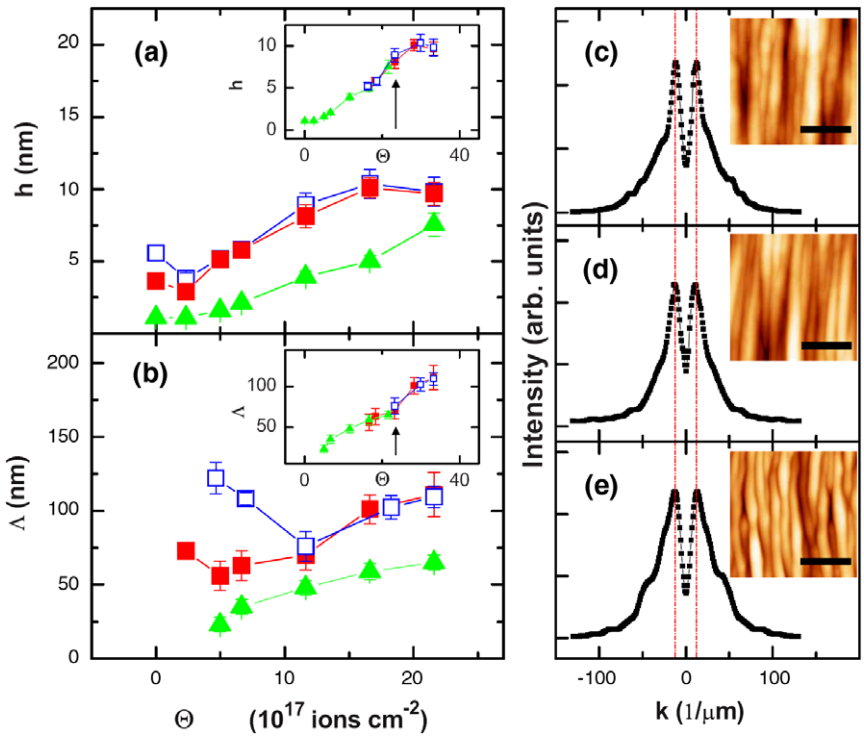

Figure 13. (a) Average amplitude h and (b) periodicity of the nanostructures Λ versus ion fluence derived from the AFM images. Red filled squares and panel (c) refer to sputter-deposited films, blue open squares and (d) to thermally evaporated, while green filled triangles and (e) to flame annealed Au films. Inset: horizontal rigid shift $\Delta\Theta = +1.2 \times 10^{18}$ ions cm^{-2} of the curves representing the rough samples (open, filled squares). (c)–(e) Topographs with the same vertical dynamic range (35 nm) of the different sample series irradiated with identical scaled ion doses. The respective 2D FFT line cuts show the equivalence of Δ. Reproduced with permission from [65]. Copyright 2008 by the American Physical Society.

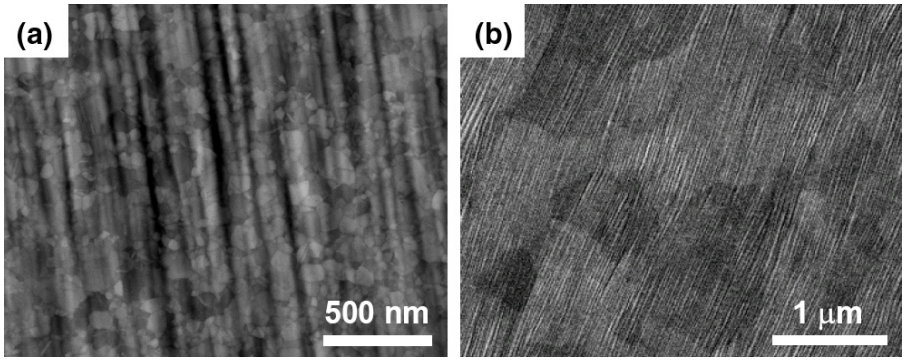

Figure 14. SEM images of ripples propagating across GBs. All the samples were sputtered with the same ion dose $\Theta = 1.2 \times 10^{18}$ ions cm^{-2}: (a) Au film grown by thermal evaporation, (b) flame annealed Au film deposited on mica substrate. The ripple topography is superimposed on the textured crystallographic contrast from the individual polycrystalline grains. Reproduced with permission from [67]. Copyright 2008, American Institute of Physics.

limitation for the propagation of a ripple pattern from grain to grain. Contrary to expectations, the SEM analysis of the sputtered films shown in [67] demonstrates that the ripple pattern does propagate coherently from grain to grain. Figure 14(a) (Au film grown by thermal evaporation) shows a situation in which the ripple wavelength is comparable to the size of individual grains (around 100 nm). Figure 14(b) (flame annealed Au film) shows a case in which the grains are much larger than the ripple wavelength. In both cases it can be clearly seen that ripples propagate coherently across the grain boundaries with just a slight orientation mismatch, which can be attributed to minute changes of in-plane rotational texture from grain to grain. The propagation length of the ripple ridges can reach or exceed several micrometres, while the phase relationship of peaks and valleys is preserved from grain to grain. Two possible mechanisms are contributing to such behaviour: an ion impinging on the surface near the grain boundary might hyperthermally activate inter-grain mass transport in the vicinity of the impact site and/or coherent ripple propagation across grain boundaries can be promoted by the shadowing mechanism active at grazing ion incidence. The topographic relief of

the ripple on a nearby grain, in fact, coherently modulates the spatial distribution of ion impact sites on the adjacent grain.

4. Tuning optical anisotropy of a polycrystalline film via localized plasmonic resonances: from surface ripples to metal nanowire arrays

In the last part of this paper we will show results which demonstrate the possibility to tailor the optical response of a metal film by controllably modifying, via IBS and controlled epitaxy, its morphology on a subwavelength scale, i.e. on a scale of dimensions which are smaller than the range of optical wavelengths. At variance with the results we have shown previously, where the functional (magnetic and catalytic) behaviour was predominantly controlled by the density and orientation of the atomic step arrays, in this case the optical functionality is predominantly originated by the shape anisotropy of the nanostructured film. In particular we find that the modification of the anisotropic optical response appears only when a rippled metal film is decomposed into a disconnected array of nanowires.

Noble metal nanoparticles exhibit unique optical properties in the visible spectral range due to the excitation of collective oscillations of conduction electrons known as localized surface plasmon resonances (LSPR) [68, 69]. The resonance frequency of surface plasmons strongly depends on the size, shape and dielectric environment of the nanoparticles, thus providing an effective way for tuning their anisotropic optical properties [70–72]. Additionally, the strong near-field enhancement due to the excitation of localized surface plasmons on the nanostructures leads to appealing phenomena such as transport and storage of electromagnetic energy below the diffraction limit (plasmon waveguiding) [73] or plasmon-enhanced sensing and spectroscopy [74, 75]. Fabrication of ordered arrays of metallic nanoparticles supported on transparent substrates has been demonstrated recurring to sequential techniques like electron-beam lithography (EBL): however, such top-down approaches are cumbersome and have a low yield, which hinders practical applications. High throughput parallel and self-organized growth approaches for the synthesis of metallic nanoparticles are thus intensely searched. One example of this possibility is shown in [76] where a silicon substrate was patterned by IBS to form a ripple array, followed by subsequent deposition of a thin noble metal Ag overlayer. By controlled thermal annealing, the continuous film breaks up, forming an ordered array of nanoclusters which are preferentially located in registry with the troughs of the ripples. The optical reflectivity of the substrate shows a polarization contrast originated from the near-field plasmonic coupling of the nanoparticles located inside the ripple troughs.

Within this context, it was recently shown [77] that a combination of self-organized IBS patterning of a dielectric substrate (glass) to form ripples, followed by metal deposition at glancing angles (to localize the metal atoms on the top of the ridges), leads to the formation of a disconnected array of noble metal nanowires (NW) supported on transparent substrates. In a different context, shadow deposition was employed to obtain the formation of arrays of ferromagnetic Co nanoparticles supported onto faceted SiGe films [78].

In figure 15(a) the glass substrate patterned by IBS presents a ripple periodicity in the range of 200 nm [79]. Subsequently, deposition of Ag is performed under glancing angle conditions, as shown in the sketch of figure 15(d), in order to selectively constrain the agglomeration of the metal atoms only on the top of the illuminated ridges of the glass template. After metal deposition, figure 15(b), one finds that the polycrystalline grains have nucleated on top of the illuminated ridge and coalesce to form a connected NW with elongations well exceeding the micrometre range (and a lateral periodicity imposed by the rippling of the glass substrate).

Far-field optical characterization (measuring transmission of polarized light in the range between 300 and 1000 nm) demonstrates that the morphological anisotropy of the metallo-dielectric substrate is reflected in a marked optical anisotropy (figure 16). The origin of the extinction peak is attributed to the excitation of localized plasmon resonances by transversely polarized light (TM mode). The optical transmittance spectra of a reference continuous Ag film (20 nm thick) conformally capping the rippled glass template (figure 16(h), continuous lines) are analogous to those of the flat Ag films (thicknesses 20, 41 and 72 nm) in figures 16(e)–(g) (open circles). For the reference films (figures 16(e)–(h)) the transmittance decreases steadily toward the infrared region due to ohmic losses and increased reflectivity; the typical UV transparency expected for a free electron model is instead hindered by the onset of the Ag interband transitions [70]. On changing light polarization from TE to TM, no evidence of dichroic absorption is observed. A similar optical behaviour (figure 16(g)) is found for the almost connected NW array shown in figure 16(c). When the polarization direction is changed from TE to TM only a slight difference in the transmittance is observed. The situation changes sharply when the NW height (and cross section) is reduced to 41 nm and, correspondingly, a well-disconnected NW array is formed (figure 16(b)).

While the transmittance for TE polarization (figure 16(f)) still resembles the behaviour of a continuous Ag film (figure 16(h)), the transmittance for TM polarization presents a localized minimum around 410 nm. This is the typical behaviour exhibited by subwavelength metal nanoparticles sustaining an LSPR [70]. For a further decrease in the height h (and cross section) of the nanowire at a nearly constant width w, we find (figure 16(e)) that the position of the plasmon resonance is redshifted to 450 nm.

These results thus demonstrate that by IBS patterning of a transparent dielectric template combined with controlled metal epitaxy it is possible to force the self-organized synthesis of laterally ordered metallic NW arrays. A fine tuning of the morphological parameters of the arrays (namely the cross section of the NW) allows us to tailor the optical and plasmonic properties of the NWs in the visible spectral range. A shift in the plasmon resonance position can also be obtained by changing the NW material (and dielectric constant), for example by employing Au instead of Ag (in this case the plasmon frequency is redshifted), or by capping the NWs with a dielectric film of appropriate dielectric constant [69].

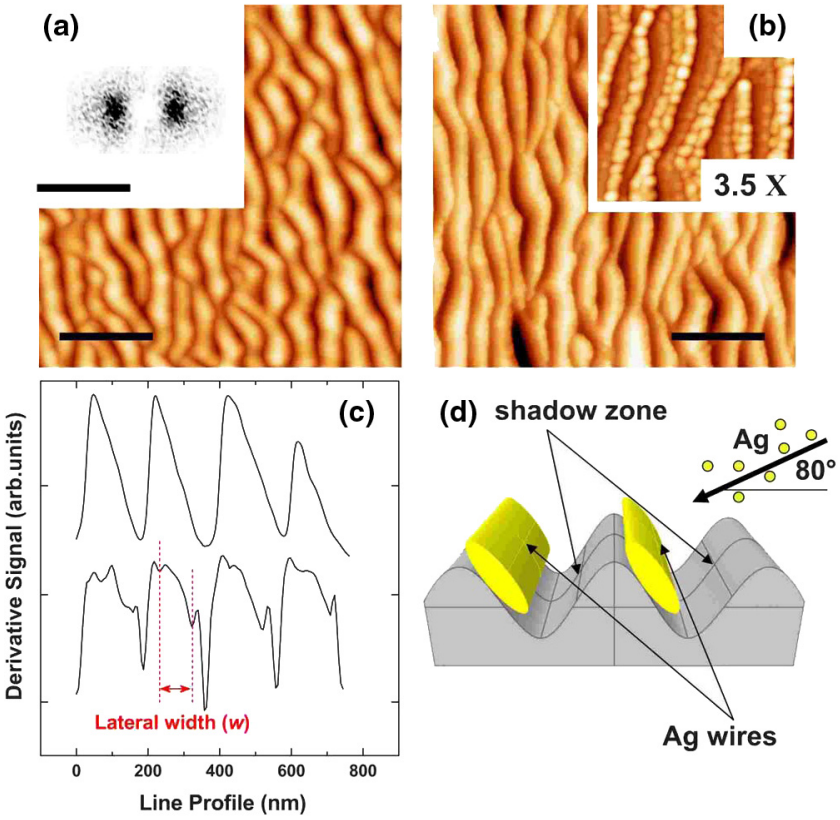

Figure 15. AFM morphology of the nanostructured glass substrate (a) before and (b) after Ag deposition (scale bars 600 nm). The insets show, respectively, a 2D FFT pattern (scale bar 15 μm^{-1}) of the glass template and a 3.5× zoom of the NW array. In panel (c) a comparison between the derivative of two line profiles before and after Ag deposition is shown. The lateral extremities of the Ag NWs are identified by the presence of additional dips indicated by dashed lines. (d) Experimental geometry adopted for the shadow deposition of Ag NWs: nucleation takes place preferentially near the top of the illuminated regions. Reproduced with permission from [77]. Copyright 2008, American Institute of Physics.

In view of functional applications in a broader range of fields, not limited to nanoplasmonics, the results presented in [77] appear of general interest since the synthesis of NWs is not restricted to a particular class of materials.

5. Conclusions

We have reviewed results relative to the formation of regular nanoscale patterns on metal substrates exposed to defocused ion beam irradiation (IBS). We have placed particular emphasis on the works which demonstrate the possibility of controllably modifying chemical, magnetic and optical properties of the material by tailoring the nanoscale morphology via IBS patterning. Crystalline metal surfaces are peculiar when compared to other substrates (like semiconductors) since even after prolonged irradiation the surface does not amorphize. Though the impact of a single ion results in the production of different kinds of point defects (vacancies and adatoms) or of extended defects (clusters) in the long term the surface morphology becomes dominated by one predominant kind of defect: atomic steps. Increasing the ion dose, regular arrays of mounds or ripples bound by steep staircases of crystalline terraces (a few atoms wide) are formed and correspondingly point defects get annihilated there with increasing efficiency.

This means that, by IBS patterning of metal surfaces, controlled dense arrays of atomic steps can be produced which are oriented either along the thermodynamic orientations (diffusive IBS regime) or along the projection of the ion beam (erosive IBS regime).

We have first recalled some of the well-established results found on single-crystal model systems, showing how the controlled modification of the atomic step termination can deeply affect chemico-physical properties. Chemical reactivity is enhanced at the highly under-coordinated sites where the local electronic density of states is modified, thus favouring electronic charge transfer to the molecular antibonding orbitals; another important material property, like magnetic anisotropy of ferromagnetic films, can also be modified by altering the distribution of atomic steps where the arrangement of atomic orbitals is modified by affecting the magnetocrystalline contribution to the energy.

We have then looked in greater detail at the more recent attempts which were focused on the extension of IBS patterning on supported polycrystalline metal films. In view of potential applications, this class of systems appears very promising in terms of low cost and of scalability in current manufacturing processes. The first commercial devices which include IBS nanostructuring into their construction steps have been disclosed. By employing IBS patterning in the

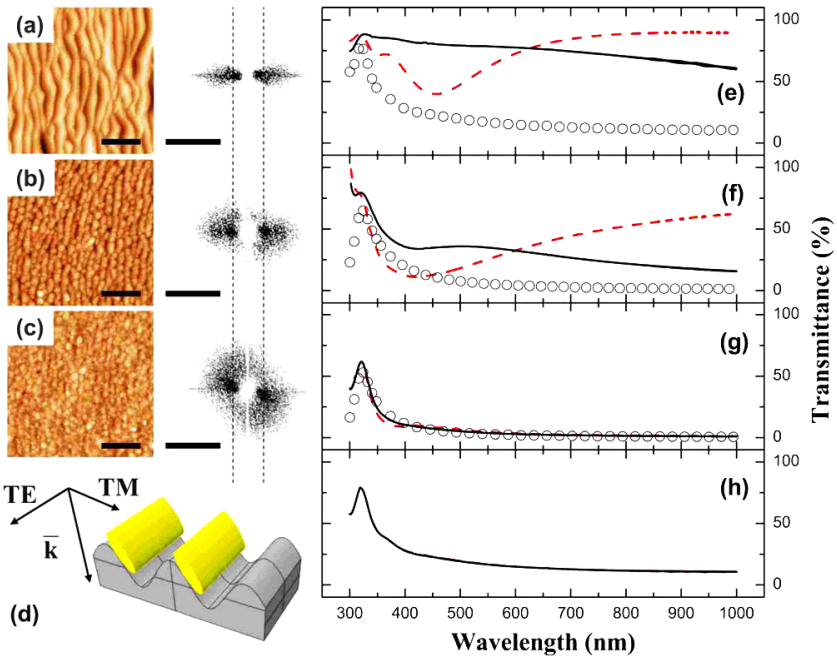

Figure 16. AFM images of the nanostructured glass surface after glancing angle Ag deposition to form nanowires. The Ag coverage (NW thickness) is: (a) $h \sim 20$ nm (b) $h \sim 41$ nm and (c) $h \sim 72$ nm. The corresponding 2D FFT patterns are plotted on the right. (d) Sketch of the incoming light polarization in the optical experiments. ((e)–(g)) Transmission optical spectra of the NW array of (a), (b) and (c), dashed/straight lines are for TM/TE polarization. Open circles: reference spectra for flat films of the same thickness. The NW aspect ratio is changed from (a) $w/h \sim 3.75$ to 1.1; correspondingly the LSPR position varies from 450 to 380 nm. Panel (h) shows the optical transmittance of a continuous Ag film supported on a rippled glass. Reproduced with permission from [77]. Copyright 2008, American Institute of Physics.

erosive regime, well-ordered ripple patterns are formed also on supported polycrystalline films, with ripple elongations well exceeding several micrometres. The presence of grain boundaries does not impede the coherent propagation of the ripple patter from grain to grain. Additionally, the primitive roughness of the films results in a faster evolution of the ripple pattern when compared to the case of the flat substrates, a promising feature in view of applications.

In the case of the IBS nanostructured polycrystalline metal films, the modification of the functional physico-chemical properties cannot be selectively modulated by growing controlled step terminations as is the case for single-crystal metal substrates, where long range crystalline order is present. The presence of rotational in-plane texture of the individual grains in fact results in a random orientation of the step arrays produced during defocused IBS patterning.

A modification of the functional properties of nanostructured polycrystalline metal films in this case is obtained by exploiting the shape anisotropy of the nanostructures. A clear example of this is provided by metal nanowires supported on templates pre-patterned by IBS. In this case the morphological anisotropy of the nanowire array is reflected in a sharp polarization-dependent modification of the optical response of the array, via excitation of localized plasmon resonances.

Acknowledgments

This work was supported by MAE under program Italia-Polonia and Italia-Slovenia and by CNISM under progetto Innesco.

References

[1] Navez M, Sella C and Chaperot D 1962 *C. R. Acad. Sci.* **254** 240
[2] Bradley R M and Harper J M E 1988 *J. Vac. Sci. Technol.* A **6** 2390
[3] Valbusa U, Boragno C and Buatier de Mongeot F 2002 *J. Phys.: Condens. Matter* **14** 8153
[4] Chan W L and Chason E 2007 *J. Appl. Phys.* **101** 121301
[5] Makeev M A, Cuerno R and Barabási A L 2002 *Nucl. Instrum. Methods Phys. Res.* B **197** 185
[6] Muñoz-García J, Castro M and Cuerno R 2006 *Phys. Rev. Lett.* **96** 086101
[7] Costantini G, Buatier de Mongeot F, Boragno C and Valbusa U 2001 *Phys. Rev. Lett.* **86** 838
[8] Michely T and Teichert C 1994 *Phys. Rev.* B **50** 11156
[9] Rusponi S, Costantini G, Buatier de Mongeot F, Boragno C and Valbusa U 1999 *Appl. Phys. Lett.* **75** 3318
[10] Costantini G, Rusponi S, Buatier de Mongeot F, Boragno C and Valbusa U 2001 *J. Phys.: Condens. Matter* **13** 5875
[11] Rusponi S, Costantini G, Boragno C and Valbusa U 1998 *Phys. Rev. Lett.* **81** 4184
[12] Molle A, Buatier de Mongeot F, Molinari A, Fuerkaiti F, Boragno C and Valbusa U 2004 *Phys. Rev. Lett.* **93** 256103
[13] Kalff M, Comsa G and Michely T 2001 *Surf. Sci.* **486** 103
[14] Ehrlich G and Hudda F G 1966 *J. Chem. Phys.* **44** 1039
[15] Schwoebel R L and Shipsey E J 1966 *J. Appl. Phys.* **37** 3682
[16] Villain J 1991 *J. Physique* I **1** 19
[17] Buatier de Mongeot F, Costantini G, Boragno C and Valbusa U 2000 *Phys. Rev. Lett.* **84** 2445
[18] Buatier de Mongeot F, Costantini G, Boragno C and Valbusa U 2002 *Europhys. Lett.* **58** 537
[19] van Dijken S, de Bruin D and Poelsema B 2001 *Phys. Rev. Lett.* **86** 4608

[20] Hansen H, Polop C and Michely T 2004 *Phys. Rev. Lett.* **92** 246106
[21] Johnson D F and Weinberg W H 1994 *J. Chem. Phys.* **101** 6289
[22] Johnson D F and Weinberg W H 1993 *Science* **261** 76
[23] Matolin V, Rebholz M and Kruse N 1991 *Surf. Sci.* **245** 233
[24] Yates J T 1995 *J. Vac. Sci. Technol.* A **13** 1359
[25] Lee S M, Lee Y H, Hwang Y G, Hahn J R and Kang H 1999 *Phys. Rev. Lett.* **82** 217
[26] Hrbek J, de la Figuera J, Pohl K, Jirsak T, Rodriguez J A, Schmid A K, Bartelt N C and Hwang R Q 1999 *J. Phys. Chem.* **48** 10557
[27] Greeley J, Nørskov J K and Mavrikakis M 2002 *Annu. Rev. Phys. Chem.* **53** 319
[28] Gambardella P, Šljivančanin Ž, Hammer B, Blanc M, Kuhnke1 K and Kern K 2001 *Phys. Rev. Lett.* **87** 056103
[29] Buatier de Mongeot F, Rocca M, Cupolillo A, Valbusa U, Kreuzer H J and Payne S H 1997 *J. Chem. Phys.* **106** 711
[30] Buatier de Mongeot F, Cupolillo A, Valbusa U and Rocca M 1997 *Chem. Phys. Lett.* **270** 345
[31] Costantini G, Buatier de Mongeot F, Rusponi S, Boragno C, Valbusa U, Vattuone L, Burghaus U, Savio L and Rocca M 2000 *J. Chem. Phys.* **112** 6840
[32] Zhang Y, Jacobs G, Sparks D E, Dry M E and Davis B H 2002 *Catal. Today* **71** 411
[33] Somorjai G A 1994 *Introduction to Surface Chemistry and Catalysis* (New York: Wiley)
[34] Zubkov T, Morgan G A and Yates J T 2002 *Chem. Phys. Lett.* **362** 181
[35] Zubkov T, Morgan G A, Yates J T, Kühlert O, Lisowski M, Schillinger R, Fick D and Jänschet H J 2003 *Surf. Sci.* **526** 57
[36] Heiz U, Vanolli F, Sanchez A and Schneider W D 1998 *J. Am. Chem. Soc.* **120** 9668
[37] Campuzano J C 1990 *The Chemical Physics of Solid Surfaces and Heterogeneous Catalysis* vol 3, ed D A King and D P Woodruff (New York: Elsevier) p 389
[38] Mavrikakis M, Baumer M, Freund H J and Nørskov J K 2002 *Catal. Lett.* **81** 153
[39] Rebholz M, Prins R and Kruse N 1991 *Surf. Sci.* R **259** L797
[40] Andersson S *et al* 1998 *J. Chem. Phys.* **108** 2967
[41] Ertl G and Freund H J 1999 *Phys. Today* **52** 32
[42] Molle A, Buatier de Mongeot F, Molinari A, Boragno C and Valbusa U 2006 *Phys. Rev.* B **73** 155418
[43] Golubovic L, Levandovsky A and Moldovan D 2002 *Phys. Rev. Lett.* **89** 266104
[44] Buatier de Mongeot F, Toma A, Molle A, Lizzit S, Petaccia L and Baraldi A 2006 *Phys. Rev. Lett.* **97** 056103
[45] Buatier de Mongeot F, Toma A, Molle A, Lizzit S, Petaccia L and Baraldi A 2007 *Nanoscale Res. Lett.* **2** 251
[46] Himpsel F J, Ortega J E, Mankey G J and Willis R F 1998 *Adv. Phys.* **47** 511
[47] Shen J and Kirschenr J 2002 *Surf. Sci.* **500** 300
[48] Johnson M T, Bloemen P J H, den Broeder F J A and de Vries J J 1996 *Rep. Prog. Phys.* **59** 1409
[49] Shinohara T, Sato T and Taniyama T 2003 *Phys. Rev. Lett.* **91** 197201
[50] Hong S C *et al* 2007 *Phys. Rev.* B **75** 172402
[51] Li F, Wang T and Ren L 2004 *J. Phys.: Condens. Matter* **16** 8053
[52] Moroni R, Sekiba D, Buatier de Mongeot F, Gonella G, Boragno C, Mattera L and Valbusa U 2003 *Phys. Rev. Lett.* **91** 167207
[53] Sekiba D, Moroni R, Gonella G, Buatier de Mongeot F, Boragno C, Mattera L and Valbusa U 2004 *Appl. Phys. Lett.* **84** 762
[54] Bisio F, Moroni R, Buatier de Mongeot F, Canepa M and Mattera L 2006 *Phys. Rev. Lett.* **96** 057204
[55] Bisio F, Moroni R, Buatier de Mongeot F, Canepa M and Mattera L 2006 *Appl. Phys. Lett.* **89** 052507
[56] Berger A, Linke U and Oepen H P 1992 *Phys. Rev. Lett.* **68** 839
[57] Chen J and Erskine J L 1992 *Phys. Rev. Lett.* **68** 1212
[58] Cowburn R P, Gray S J and Bland J A C 1997 *Phys. Rev. Lett.* **79** 4018
[59] Wu Y Z, Won C and Qiu Z Q 2002 *Phys. Rev.* B **65** 184419
[60] Zhang K, Rotter F, Uhrmacher M, Ronning C, Krauser J and Hofsäss H 2007 *New J. Phys.* **9** 29
[61] Zhang K, Uhrmacher M, Hofsäss H and Krauser J 2008 *J. Appl. Phys.* **103** 083507
[62] Carey M J, Childress J R, Fullerton E E and Maat S 2008 Method for manufacturing a magnetic read sensor employing oblique etched underlayers for inducing uniaxial magnetic anisotropy in hard magnetic bias layers *US Patent Specification* 7360300
[63] Karmakar P and Gose D 2004 *Surf. Sci.* **554** L101
[64] Stepanova M and Dew S K 2006 *J. Vac. Sci. Technol.* B **24** 592
[65] Toma A, Chiappe D, Šetina Batic B, Godec M, Jenko M and Buatier de Mongeot F 2008 *Phys. Rev.* B **78** 153406
[66] Davidovitch B, Aziz M J and Brenner M P 2007 *Phys. Rev.* B **76** 205420
[67] Toma A, Šetina Batic B, Chiappe D, Boragno C, Valbusa U, Godec M, Jenko M and Buatier de Mongeot F 2008 *J. Appl. Phys.* **104** 10431
[68] Ozbay E 2006 *Science* **311** 189
[69] Kreibig U and Vollmer M 1995 *Optical Properties of Metal Clusters* (Berlin: Springer)
[70] Muskens O, Christofilos D, Del Fatti N and Vallée F 2006 *J. Opt. A: Pure Appl. Opt.* **8** S264
[71] Noguez C 2007 *J. Phys. Chem.* C **111** 3806
[72] Kooij E S and Poelsema B 2006 *Phys. Chem. Chem. Phys.* **8** 3349
[73] Maier S A, Kik P G, Atwater H A, Meltzer S, Harel E, Koel B E and Requicha A A G 2003 *Nat. Mater.* **2** 229
[74] Yang Y, Xiong L, Shi J and Nogami M 2006 *Nanotechnology* **17** 2670
[75] Suzuki M, Maekita W, Wada Y, Nakajima K, Kimura K, Fukuoka T and Mori Y 2006 *Appl. Phys. Lett.* **88** 203121
[76] Oates T W H, Keller A, Facsko S and Muecklich A 2007 *Plasmonics* **2** 47
[77] Toma A, Chiappe D, Massabò D, Boragno C and Buatier de Mongeot F 2008 *Appl. Phys. Lett.* **93** 163104
[78] Teichert C, Barthel J, Oepen H P and Kirschner J 1999 *Appl. Phys. Lett.* **74** 588
[79] Toma A, Buatier de Mongeot F, Buzio R, Firpo G, Bhattacharyya S R, Boragno C and Valbusa U 1996 *Nucl. Instrum. Methods* B **115** 440